Equivalent Circuit Model for a Large Array of Coupled Piezoelectric Micromachined Ultrasonic Transducers With High Emission Performance

Tingzhong Xu, Libo Zhao, Zhuangde Jiang, Shuaishuai Guo, Zhikang Li, Ping Yang, Guoxi Luo, Lin Sun, and Liangchi Zhang

***Abstract*— In this article, an analytical equivalent circuit model is established for the piezoelectric micromachined ultrasonic transducer (PMUT) cell and array with a combination of the annular and circular diaphragms used for structural optimization and complex array design. Based on this model, a comprehensive analysis is conducted on the acoustic-structural coupling of an annular and circular diaphragm-coupled PMUT (AC-PMUT) with a new excitation method. The model-derived results are in good agreement with the simulation and experimental results. Then, an optimized design has been presented to achieve high-output pressure and a good array working performance. In summary, a comparison of the array working performance is conducted between the arrays that consist of AC-PMUTs and traditional circular diaphragm PMUTs (C-PMUTs). The results indicate that the AC-PMUT array has a much lower crosstalk effect than that of the traditional C-PMUT array. By this means, the AC-PMUT array can fully use the high vibration amplitude achieved by each AC-PMUT cell to improve its output ability. As a result, the highest ultrasonic output pressure generated by the AC-PMUT array in its resonant condition can achieve an increase of 155%, compared with that generated by the C-PMUT array.**

Manuscript received April 15, 2020; accepted June 30, 2020. Date of publication July 9, 2020; date of current version February 24, 2021. This work was supported in part by the National Natural Science Foundation of China under Grant 51875449, Grant 51890884, and Grant 91748207, in part by the Shaanxi Province Natural Science Basic Research Project under Grant 2019JC-06, and in part by the Australian Research Council Discovery Project under Grant DP170100567. *(Corresponding authors: Libo Zhao; Zhikang Li.)*

Tingzhong Xu is with the State Key Laboratory for Manufacturing Systems Engineering, International Joint Laboratory for Micro/Nano Manufacturing and Measurement Technologies, Collaborative Innovation Center of Suzhou Nano Science and Technology, School of Mechanical Engineering, Xi'an Jiaotong University, Xi'an 710049, China, and also with the School of Mechanical and Manufacturing Engineering, University of New South Wales, Sydney, NSW 2052, Australia (e-mail: tingzhong.xu@student.unsw.edu.au; tingzhongxu@163.com).

Libo Zhao, Zhuangde Jiang, Shuaishuai Guo, Zhikang Li, Ping Yang, Guoxi Luo, and Lin Sun are with the State Key Laboratory for Manufacturing Systems Engineering, International Joint Laboratory for Micro/Nano Manufacturing and Measurement Technologies, Collaborative Innovation Center of Suzhou Nano Science and Technology, School of Mechanical Engineering, Xi'an Jiaotong University, Xi'an 710049, China (e-mail: libozhao@mail.xjtu.edu.cn; zdjiang@mail.xjtu.edu.cn; gsscth@stu.xjtu.edu.com; zhikangli@xjtu.edu.cn; ipe@xjtu.edu.cn; luoguoxi@xjtu.edu.cn; sunlinxjtu@126.com).

Liangchi Zhang is with the School of Mechanical and Manufacturing Engineering, University of New South Wales, Sydney, NSW 2052, Australia (e-mail: liangchi.zhang@unsw.edu.au).

This article has supplementary downloadable material available at ieeexplore.ieee.org, provided by the authors.

Digital Object Identifier 10.1109/TUFFC.2020.3008179

***Index Terms*— Coupled vibration, crosstalk effect, high emission performance, piezoelectric micromachined ultrasonic transducers (PMUTs), ultrasonic output pressure.**

I. Introduction

ULTRASONICS has been playing significant roles in almost all aspects of our life, including industrial nondestructive testing (NDT) [1], [2], medical treatment [3]–[5], and consumer electronics [6]–[8]. Although advances have been achieved by bulk ultrasonic systems based on the thickness vibration mode, the laborious manufacturing process limits the realization of cost-effectiveness, small form factor, and 2-D arrays for advanced ultrasonic imaging [9]–[12]. As an alternative, the microelectromechanical system (MEMS)-based ultrasonic transducers are showing their advantages in cost-effective manufacturing with large volume, advanced ultrasonic array design, and device miniaturization [11], [13].

Recently, piezoelectric micromachined ultrasonic transducers (PMUTs) have received significant attention in developing MEMS-based ultrasonic transducers. In order to achieve a high signal-to-noise ratio (SNR) during detection, ultrasonic emission performance must be improved [14]–[16]. Wang *et al.* [14] increased the output pressure by 76% by introducing isolation trenches at the diaphragm edge of each PMUT cell. Akhbari *et al.* [15] presented a PMUT cell with dual-electrode double piezoelectric layers to increase the ultrasonic emission sensitivity by 400%, compared with the state of the art. Akhbari *et al.* [16] designed a PMUT cell with curved aluminum nitride (AlN) diaphragms with a static displacement of 50 times higher than that of a flat diaphragm with the same diameter. Shelton *et al.* [17] introduced a PMUT cell with an impedance-matching tube, which increased the sound pressure level by 350%. Eovino *et al.* [18], [19] presented an annular diaphragm PMUT (A-PMUT) cell with a high-output ability, which achieved an increase of 900% in directionality, compared with traditional circular diaphragm PMUTs (C-PMUTs). Wang *et al.* [20] presented an annular–circular diaphragm-coupled PMUT to make the cell diameter match with the acoustic wave and achieved 1.9 times higher emission sensitivity than the traditional C-PMUTs. However, the above-discussed performance parameters of the PMUTs were not obtained in an array.

Considering the small dimension of each PMUT cell, many of them must be connected in parallel to form a larger array to achieve a practical value. An array analysis model is required to examine their performance in depth. Bayran *et al.* [21] concluded that the dispersive guided modes propagating in the fluid–solid interface serve as the working mechanism of acoustic interaction through experimental characterization and FEM analysis. Meynier *et al.* [22] presented a time-efficient simulation based on the separate calculations of the self- and mutual-radiation impedances of a CMUT array. Berthillier *et al.* [23] used a Rayleigh integral to establish an efficient simulation program considering the multivibration modes of the circular diaphragm and to reveal the heavy acoustic interaction among the cells in an array. Oguz *et al.* [24] introduced an equivalent circuit model for a CMUT cell working in an array, including the self- and mutual-radiation impedances of a circular diaphragm in its bending vibration mode.

In a closely packed array, the acoustic interactions among cells lead to different acoustic loadings on each cell, which is called crosstalk [25]–[28]. The crosstalk degrades the performance of the transducers in certain applications, such as medical imaging and diagnosis [29]. Several crosstalk-relieving methods were presented on the basis of the above-mentioned array analysis methods. An early approach was based on the damping method [30]. By adding losses to each cell in the array, the spurious resonances caused by crosstalk can be significantly suppressed. However, this method impairs the emission sensitivity of the MUTs. Then, the active cancellation methods based on the excitation control of each cell were presented [31], [32]. However, these methods were based on the vibration displacement field of each cell in the array, which was difficult to derive by simulation or experiments. They would also complicate the circuit design for the transducers.

In the field of PMUTs, Akhbari *et al.* [33] presented an equivalent circuit model for a single PMUT cell with a spherical-shaped diaphragm working in an array, which realized the array performance analysis of the PMUTs. Wang and Horsley [34] investigated the edge-wave-induced crosstalk effect by the experimental and analytical methods and the transmit time-response influenced by the strong acoustic coupling in the densely packed PMUTs. However, none of the works presented an effective way to handle the crosstalk effect.

In this article, an analytical equivalent circuit model is established for the PMUT cell and array with a combination of the annular and circular diaphragms. The model validity is examined by simulations and experimental results. Based on the proposed model, a PMUT cell structure composed by a pair of coaxially positioned annular and circular diaphragms is presented. The excitation phases of these two diaphragms are separately controlled to enhance the vibration coupling between them. Based on the continuity equation of the fluid, the crosstalk effect between the coaxially positioned annular and circular diaphragms within one cell can not only reduce the crosstalk intensity among different cells but also achieves a high ultrasonic emission performance.

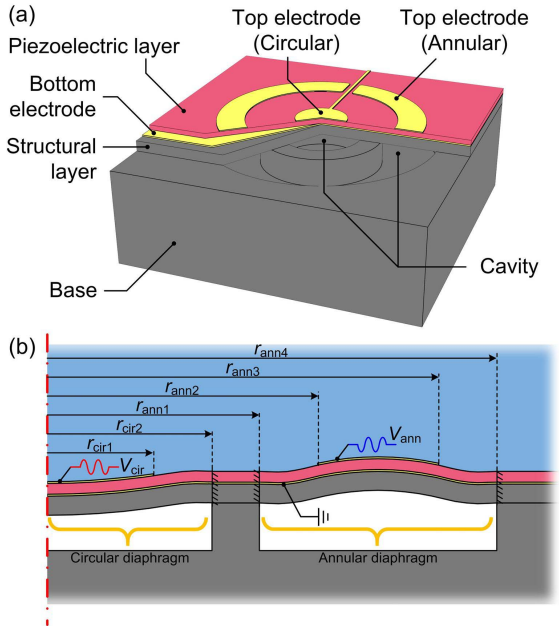

Fig. 1. Schematics of (a) AC-PMUT cell and (b) its sectional view.

In addition, an optimization design for the annular and circular diaphragm-coupled PMUT (AC-PMUT) cell has been conducted by using the proposed equivalent circuit model. Finally, a comparison of emission performance is conducted between the C-PMUT array and the proposed AC-PMUT array, verifying that the AC-PMUT array has a better emission performance and a lower crosstalk intensity.

II. Basic Circuit Model for AC-PMUT Cell

A. Structural Design for AC-PMUT Cell

The schematics of the AC-PMUT cell are illustrated in Fig. 1. From bottom to top, both diaphragms are composed of a structural layer, bottom electrode, piezoelectric layer, and top electrodes. The polarization direction of the piezoelectric layer is perpendicular to the diaphragm surface. As an ultrasound transmitter, an alternating electric field along the polarization direction will be applied between the top and bottom electrodes to drive the diaphragm vibration and emit ultrasound. In addition, these two diaphragms can be regarded as mechanically separated but acoustically coupled.

B. Equivalent Circuit Model for a Single AC-PMUT Cell

Given the considerably smaller structural dimension of a PMUT cell than that of the acoustic wavelength, a lumped element model can be used to analyze and predict its acoustic behavior [27], [35], [36]. The lumped element model is presented using an equivalent circuit, as shown in Fig. 2. In the circuit, C_{cir} and C_{ann} are the clamped dc capacitances between the top and bottom electrodes, η_{cir} and η_{ann} are the electromechanical transduction ratios, $u_{\mathrm{cir}\,i}$ and $u_{\mathrm{ann}\,i}$ are the volumetric vibration velocities, Z_{Cm} and Z_{Am} are the mechanical impedances, and z_{cir} and z_{ann} are the self-radiation impedances of the circular and annular diaphragms, respectively [37]–[39].

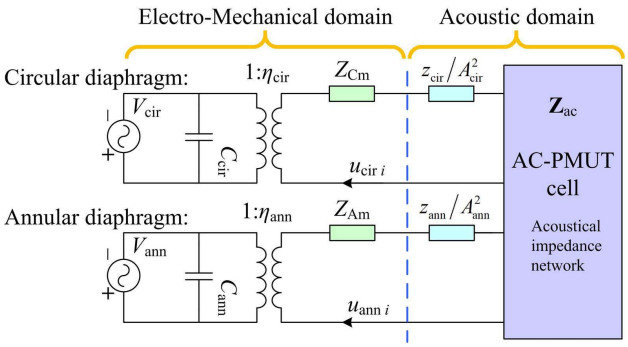

Fig. 2. Equivalent circuit model for a single AC-PMUT cell.

Moreover, Z_{AC} is the interaction matrix between the coaxially positioned annular and circular diaphragms induced by acoustic coupling [27]. The relationship between the interaction pressure loaded on each diaphragm and the volumetric vibration velocity of the annular and circular diaphragms can be presented as follows:

$$\begin{bmatrix} p_{ca} \\ p_{ac} \end{bmatrix} = \mathbf{Z}_{ac} \cdot \begin{bmatrix} u_{cir\,i} \\ u_{ann\,i} \end{bmatrix} = \begin{bmatrix} 0 & \dfrac{z_{ac}}{A_{cir} \cdot A_{ann}} \\ \dfrac{z_{ac}}{A_{ann} \cdot A_{cir}} & 0 \end{bmatrix} \begin{bmatrix} u_{cir\,i} \\ u_{ann\,i} \end{bmatrix} \tag{1}$$

where p_{ca} denotes the interaction pressure from the annular diaphragm acting on the circular diaphragm surface, and vice versa, A_{cir} and A_{ann} are the effective vibration areas of the circular and annular diaphragms, respectively, which make the equivalent piston vibration achieve the same volumetric displacement as the proposed circular and annular diaphragms [33], [37], and z_{AC} is the mutual radiation impedance between the coaxially positioned annular and circular diaphragms.

The calculation of the equivalent circuit can be divided into two domains, as shown in Fig. 2. The electromechanical domain of the AC-PMUT cell can be simplified as the calculation of a pair of mechanically independent piezoelectric-driven monomorph annular and circular plates that consist of an AlN piezoelectric layer and a silicon structural layer, as discussed in detail in previous studies [37]–[40]. The calculation of the acoustic domain consists of three parts: the self-radiation impedance of the circular diaphragm, self-radiation impedance of the annular diaphragm, and mutual-radiation impedance coupling the two diaphragms.

The self-radiation impedance of the circular diaphragm can be calculated as an equivalent baffled piston with the same volumetric displacement, as discussed in detail in previous studies [33], [41]. In addition, the self-radiation impedance of the annular diaphragm can also be calculated as an equivalent baffled piston with the same volumetric displacement, as discussed in detail in previous studies [37].

According to the effective lateral dimensions of the circular and annular diaphragms, the circular area having an effective radius of r_{eff4} can be divided into several circular and annular regions like a jigsaw puzzle, as shown in Fig. 3. Assuming that all jigsaw areas can vibrate with a spatially uniform velocity

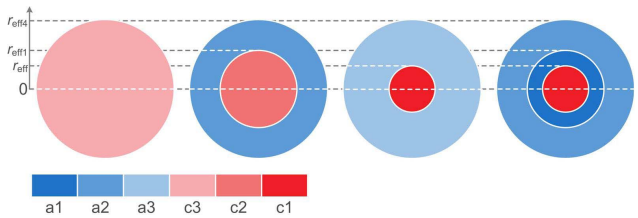

Fig. 3. Jigsaw area projected by the effective vibration areas of the annular and circular diaphragms.

TABLE I
SUMMARY OF THE STRUCTURAL PARAMETERS OF THE ANALYZED AC-PMUT [20]

Symbol	Value	Unit	Description
r_{cir2}-r_{ann1}-r_{ann4}	30-50-90	μm	Structure I
	32-48-92	μm	Structure I with fabrication error
	30-50-95	μm	Structure II
	32-48-97	μm	Structure II with fabrication error
r_{cir1}	$0.65 \cdot r_{cir2}$	μm	Top electrode radius of circular diaphragm
$r_{ann3} - r_{ann2}$	$0.55 \cdot (r_{ann4} - r_{ann1})$	μm	Top electrode width of annular diaphragm
h_1	2500	nm	Non-active layer thickness
h_2	1000	nm	Piezoelectric layer thickness

All symbols are illustrated in Fig. 1.

in a rigid baffle area, the radiation impedances of regions c2, a3, and c3 can be presented as follows [42]:

$$z_{c2} = z_{a1} + z_{c1} + 2 \cdot z_{a1\,c1} \tag{2}$$

$$z_{a3} = z_{a1} + z_{a2} + 2 \cdot z_{a1\,a2} \tag{3}$$

$$z_{c3} = z_{a2} + z_{a1} + z_{c1} + 2 \cdot z_{a1\,a2} + 2 \cdot z_{a2\,c1} + 2 \cdot z_{a1\,c1} \tag{4}$$

where an expression such as z_{AB} represents the mutual radiation impedance between regions A and B, $z_{c\,i}$ represents the self-radiation impedance of the circular region ci, and $z_{a\,i}$ represents the self-radiation impedance of the annular region ai.

By substituting (2) and (3) into (4), the expression for mutual radiation impedance between the coaxially positioned circular and annular diaphragms can be obtained as follows:

$$z_{ac} = z_{a2c1} = (z_{c3} - z_{a3} - z_{c2} + z_{a1})/2. \tag{5}$$

C. Cell Model Verification

To verify the model, the results derived from the proposed model are compared with the simulation and experimental results presented in [20]. However, the top electrodes of the annular and circular diaphragms presented in [20] are connected, and the two diaphragms can only be excited in the same phase. The frequency response of the center displacement sensitivity of the circular and annular diaphragms is analyzed in Fluorinert FC-70 ($\rho = 1940$ kg/m^3 and $c = 687$ m/s [20], [34]). In addition, according to the SEM photograph presented in [20, Fig. 2], the etching errors should be considered in the model verification. Tables I and II summarize the detailed structural and material parameters, respectively.

TABLE II
SUMMARY OF THE MATERIAL PROPERTIES OF THE ANALYZED AC-PMUT

Symbol	Value	Unit	Description
Y_1	170	GPa	Young's modulus of Si
Y_2	340	GPa	Young's modulus of AlN
υ_1	0.28	–	Poisson's ratio of Si
υ_2	0.3	–	Poisson's ratio of AlN
ρ_1	2329	kg/m^3	Density of Si
ρ_2	3300	kg/m^3	Density of AlN
d_{31}, d_{32}	2.2	pm/V	Piezoelectric coefficient of AlN

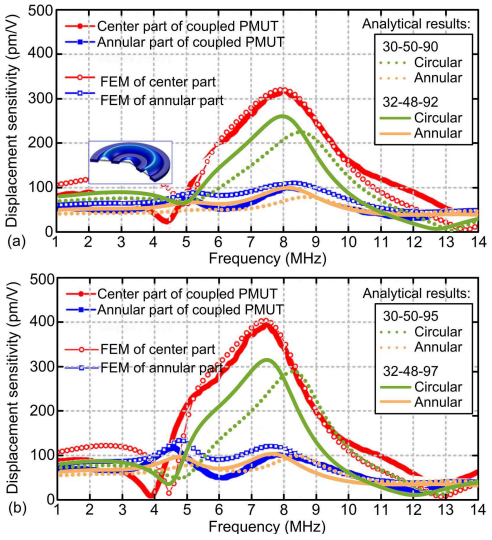

Fig. 4. Comparisons of the displacement sensitivity between the proposed model and the experimental results [20]. (a) Comparison with the 30–50–90 structure. (b) Comparison with the 30–50–95 structure.

TABLE III
SUMMARY OF THE STRUCTURAL PARAMETERS OF THE PROPOSED AC-PMUT

Symbol	Value	Unit	Description
r_{cir2}-r_{ann1}-r_{ann4}	52-87-166	μm	Proposed AC-PMUT structure
r_{cir1}	$0.65{\cdot}r_{cir2}$	μm	Top electrode radius of circular diaphragm
$r_{ann3} - r_{ann2}$	$0.55{\cdot}(r_{ann4} - r_{ann1})$	μm	Top electrode width of annular diaphragm
h_1	3000	nm	Non-active layer thickness
h_2	850	nm	Piezoelectric layer thickness

All symbols are illustrated in Fig. 1.

Fig. 4 provides a comparison of the two types of structures and their versions considering the etching errors. The frequency-response profiles derived from the proposed model agree well with the experimental results presented in [20]. The smaller amplitude value of the proposed model can be caused by the piezoelectric coefficient difference of AlN between the model and the real experiment.

Acoustic field analysis is then conducted in water for the proposed AC-PMUT by using different excitation conditions.

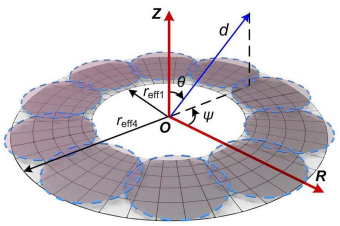

Fig. 5. Acoustic model based on equivalent piston for annular diaphragm.

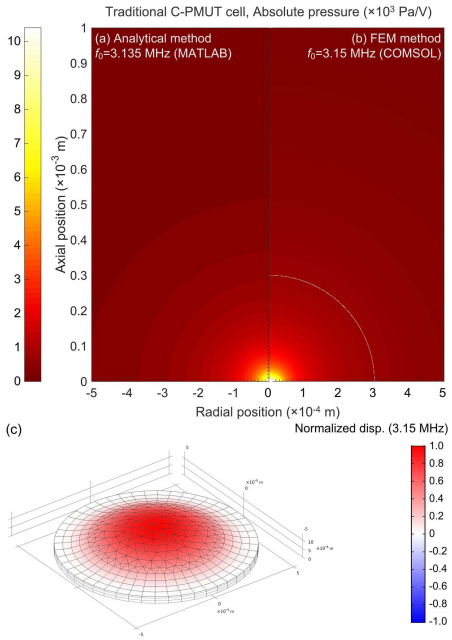

Fig. 6. Spatial distribution of the output pressure and its corresponding vibration mode generated by the C-PMUT cell ($r_{ann1} = 52$ μm) in its resonant condition. (a) Model-derived result. (b) FEM-derived result. (c) Resonant vibration mode derived by Comsol simulation.

Table III presents the structural parameters of the annular and circular diaphragms used in the verification.

The acoustic field generated by the circular diaphragm can be calculated through an acoustic field generated by an equivalent circular piston, as presented in [33] and [41].

As shown in Fig. 5, the acoustic field generated by the annular diaphragm can be calculated by an acoustic field generated by an equivalent annular piston with an effective inner radius r_{eff1} and an outer radius r_{eff4}

$$p_{ann} = jkr_{mean}\omega\rho_0 c_0 \upsilon_{ann} \frac{e^{j\left(\omega t - k\sqrt{d^2+r_{mean}^2}\right)}}{\sqrt{d^2+r_{mean}^2}} \cdot D_{ann}(\theta), \quad d > R_{Rayl} \tag{6}$$

$$D_{ann}(\theta) = \frac{2}{1-(r_{eff1}/r_{eff4})^2} \cdot \frac{J_1(kr_{eff4}\sin\theta) - (r_{eff1}/r_{eff4})J_1(kr_{eff1}\sin\theta)}{kr_{eff4}\sin\theta} \tag{7}$$

$$R_{Rayl} = kR_{eff4}^2/2 \tag{8}$$

where υ_{ann} is equal to $u_{ann\,i}/[\pi \cdot (r_{eff4}^2 - r_{eff1}^2)]$.

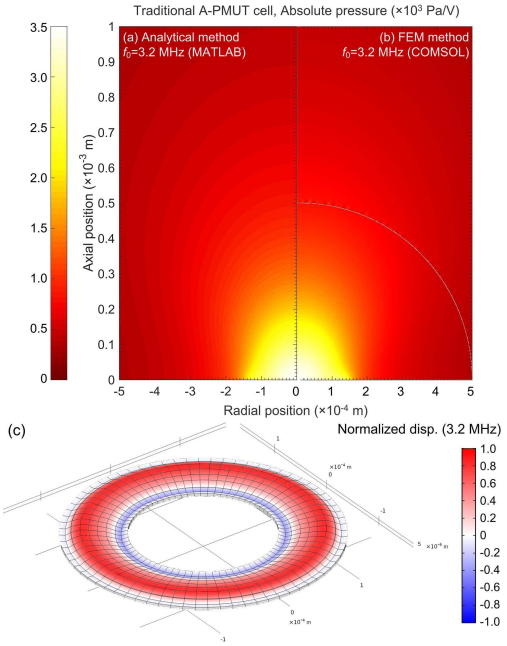

Fig. 7. Spatial distribution of the output pressure and its corresponding vibration mode generated by the A-PMUT cell ($r_{ann1} = 87\ \mu$m and $r_{ann4} = 166\ \mu$m) in its resonant condition. (a) Model-derived result. (b) FEM-derived result. (c) Resonant vibration mode derived by Comsol simulation.

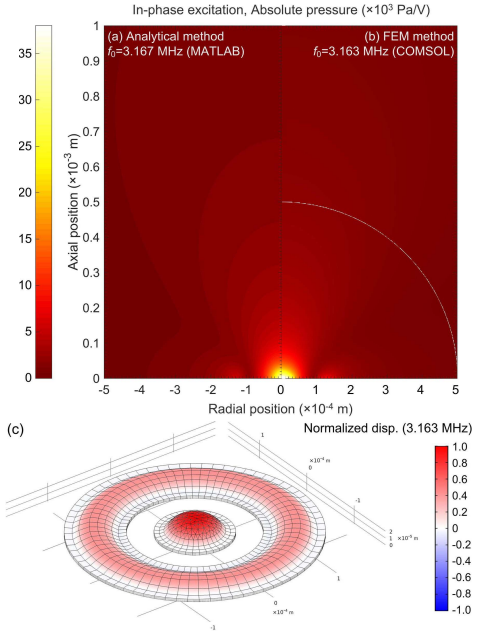

Fig. 8. Spatial distribution of the output pressure and its corresponding vibration mode generated by the in-phase-excited AC-PMUT cell in its resonant condition. (a) Model-derived result. (b) FEM-derived result. (c) Resonant vibration mode derived by Comsol simulation.

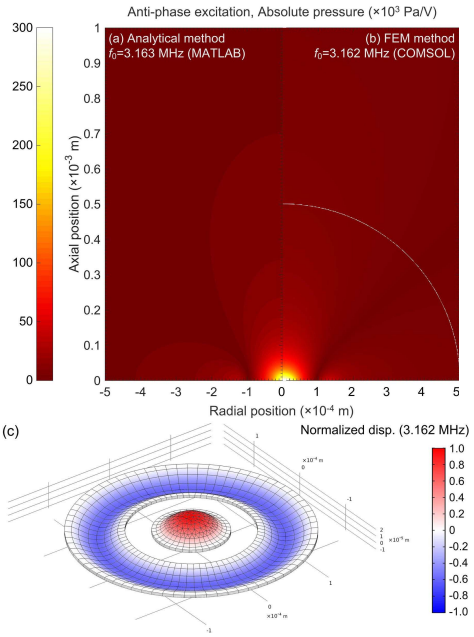

Fig. 9. Spatial distribution of the output pressure and its corresponding vibration mode generated by the antiphase-excited AC-PMUT cell in its resonant condition. (a) Model-derived result. (b) FEM-derived result. (c) Resonant vibration mode derived by Comsol simulation.

However, (6) is not suitable for the nonaxial acoustic calculation in the near field. When it comes to the near-field calculation, the annular diaphragm can be equivalent to an annular array consisting of N_0 circular pistons. The near-field acoustic field can be a superposition of the acoustic field generated by these equivalent pistons. In addition, the equivalent method of the piston array has been discussed in Section IV-A.

Figs. 6–9 present the acoustic model verification for the C-PMUT cell ($r_{cir2} = 52\ \mu$m), A-PMUT cell ($r_{ann1} = 87\ \mu$m and $r_{ann4} = 166\ \mu$m), and the in-phase-excited and antiphase-excited proposed AC-PMUT cells at their resonant frequencies under ± 1 V excitation. The vibration-mode shape of the diaphragms has also been presented for each corresponding emission condition. According to the comparison, the model-derived acoustic results agree well with the FEM-derived ones.

Then, the output pressure distributed along the axis of each cell is compared, as displayed in Fig. 10. It can be seen that the antiphase-excited AC-PMUT cell achieves the highest output pressure. The directivities of these cells are shown in Fig. 11, which show that the A-PMUT cell and the in-phase- and antiphase-excited AC-PMUT cells having larger apertures achieve a much better directivity than that of the C-PMUT cell.

III. Structural Optimization for the AC-PMUT

An optimization is conducted for the AC-PMUT cell in this section. On the basis of fabrication capability, the thicknesses of the AlN and Si layers are determined as 850 and 3000 nm, respectively. A gap of 35 μm is allocated between the coaxially positioned annular and circular diaphragms to ensure the bonding quality of the cavity-SOI. Considering the requirements of medical applications [43], the working frequency of the proposed AC-PMUT cell is set to be approximately 3 MHz in water. To meet the demand of the frequency, the circular diaphragm radius is set to be 52 μm. By this means, the inner radius of the annular diaphragm is determined as 87 μm. Still,

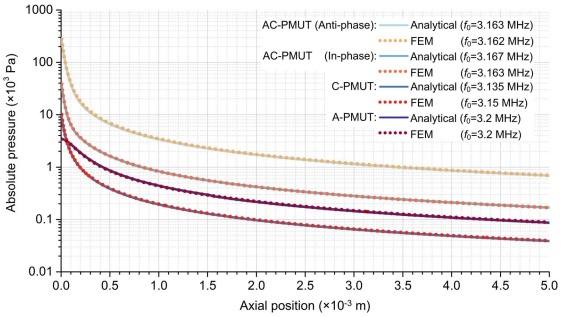

Fig. 10. Comparison of axial pressure distributions among the C-PMUT cell, the A-PMUT cell, and the in-phase-excited and antiphase-excited AC-PMUT cells.

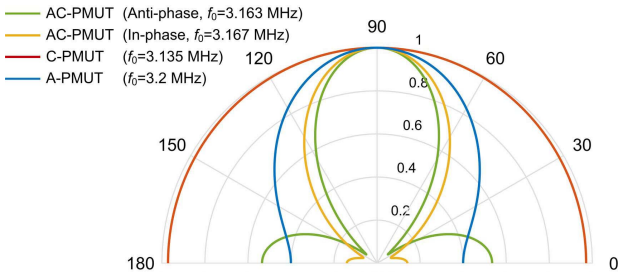

Fig. 11. Comparison of directivities among the C-PMUT cell, the A-PMUT cell, and the in-phase-excited, and antiphase-excited AC-PMUT cells.

the outer radius of the annular diaphragm and the excitation phase difference between the coaxially positioned annular and circular diaphragms need to be determined. Therefore, a traversing optimization is conducted by testing the output sensitivity of an AC-PMUT cell with different combinations between the excitation phase difference and outer radius of the annular diaphragm.

The output power sensitivity of an AC-PMUT cell with different annular diaphragm widths ($r_{ann4} - r_{ann1}$) is analyzed under various excitation phase differences between the two diaphragms. Fig. 12(a) shows the frequency responses' envelopes of the AC-PMUT cell in the output power sensitivity generated by the cell with various annular diaphragm widths ($r_{ann4} - r_{ann1}$), under a determined excitation phase difference between the circular and annular diaphragms ranging from 0° to 360°. Fig. 12(a) indicates that the maximum output power sensitivity can be achieved when the excitation phase difference is approximately 180°. Therefore, the circular and annular diaphragms are set in an antiphase excitation mode to simplify the excitation circuit design. Then, the frequency responses' envelopes of the AC-PMUT with various annular diaphragm widths, ranging from 65 to 95 μm, under the antiphase excitation condition have been analyzed in detail in Fig. 12(b) and (c), which indicates that the one with an annular diaphragm width of 79 μm can achieve the highest output sensitivity.

Fig. 13 presents the relationship between the resonant frequency similarity and the output power ability of the AC-PMUT cell under the antiphase-excitation condition, which indicates that the antiphase-excited AC-PMUT cell can achieve a higher output sensitivity when the circular

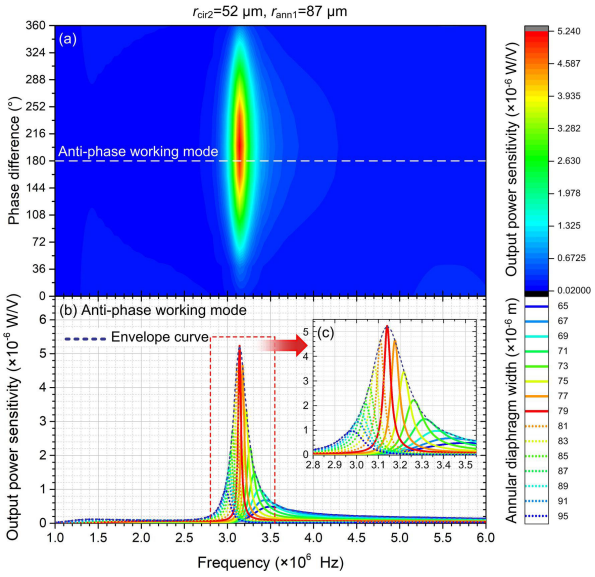

Fig. 12. Traversing optimization for a single AC-PMUT cell. (a) Frequency responses' envelopes of an AC-PMUT cell with various annular diaphragm widths, under a determined excitation phase difference ranging from 0° to 360°. (b) Frequency responses of the AC-PMUT with various annular diaphragm widths under the antiphase excitation condition. (c) Enlarged view of the frequency response around the resonant peaks.

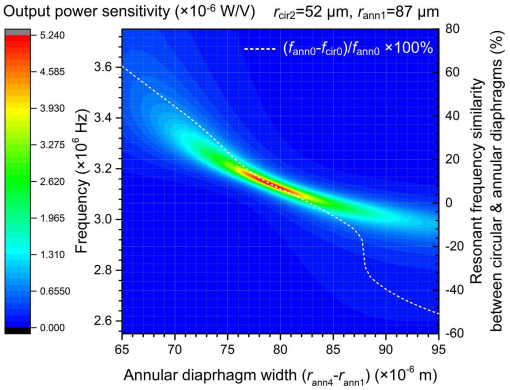

Fig. 13. Relationship between the resonant frequency similarity and the output power sensitivity of the AC-PMUT cells under the antiphase-excitation condition.

and annular diaphragms achieve a close value of resonant frequency.

Based on the fluid-structure coupling effect [44], the vibration amplitudes of the two diaphragms are amplified under the antiphase-excitation working mode. Fig. 14 presents the frequency response of the output pressure at 700 μm in front of the AC-PMUT cell corresponding to the annular diaphragm with a specific width. In accordance with the results in Fig. 12, an output pressure peak occurs at the resonant frequency when the annular width is approximately 79 μm. However, because of the antiphase vibration between the two diaphragms, a certain amount of output power produced by each diaphragm will offset with each other. After getting the vibration results from the model of a single cell, the vibration results of the circular and annular diaphragms can

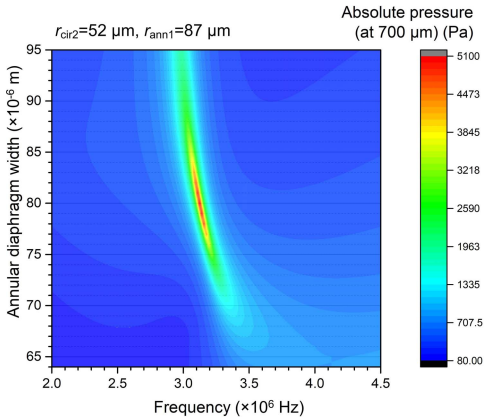

Fig. 14. Output pressure (at 700 μm) versus frequency response of the AC-PMUT cell with different annular diaphragm widths excited in an antiphase mode.

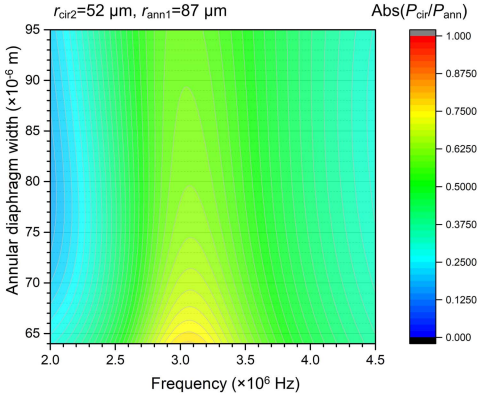

Fig. 15. Abs(P_{cir}/P_{ann})-frequency response of the AC-PMUT cell with different annular diaphragm widths, where P_{cir} and P_{ann} denote the output pressures contributed by the circular and annular diaphragms, respectively, in the antiphase working mode.

be extracted to calculate the output pressure contributions of the two diaphragms, respectively. Fig. 15 presents the frequency response of the ratio between the absolute output pressures generated by the circular and annular diaphragms, which indicates that the annular diaphragm is a contributor to the output pressure, whereas the vibration of the circular diaphragm can offset half of the pressure contributed by the annular diaphragm.

Although a large vibration amplitude is preferable to increase the output ability of the PMUT, the vibration amplitude should be limited under a safety value to ensure all the material consisting of the diaphragm work in their elastic deformation domain to guarantee the working stability of the PMUT. Based on the boundary condition of these two diaphragms, the maximum stress will concentrate at the clamped edge of the diaphragm, dominated by tensile stress [45]. The stress value of the diaphragm can be presented as follows:

$$\sigma_{\text{radi}} = -\frac{Ez_{\text{h}}}{1-\mu^2}\left(\frac{\partial^2 w}{\partial^2 r} + \mu\frac{\partial^2 w}{\partial^2 (r\theta)}\right) \tag{9}$$

$$\sigma_{\text{tage}} = -\frac{Ez_{\text{h}}}{1-\mu^2}\left(\frac{\partial^2 w}{\partial^2 (r\theta)} + \mu\frac{\partial^2 w}{\partial^2 r}\right) \tag{10}$$

where σ_{radi} and σ_{tage} are the stresses along the radial and tangential directions, respectively, z_{h} is the vertical distance to the neutral plane, E and μ are Young's modulus and Poisson's ratio of the material, respectively, and w is the diaphragm deflection.

Considering that the vibration modes of the annular and circular diaphragms of an individually working AC-PMUT cell are axisymmetric, the second derivative of the diaphragm deflection along the tangential direction is equal to 0. This makes the value of σ_{tage} much smaller than that of σ_{radi}. In addition, considering that the endurance limit of AlN (168–248 MPa) [46] is much larger than that of Si (130–150 MPa) [47], the maximum tensile stress σ_{radi} of the silicon structure is used as the judging criteria and need to be kept under 130 MPa.

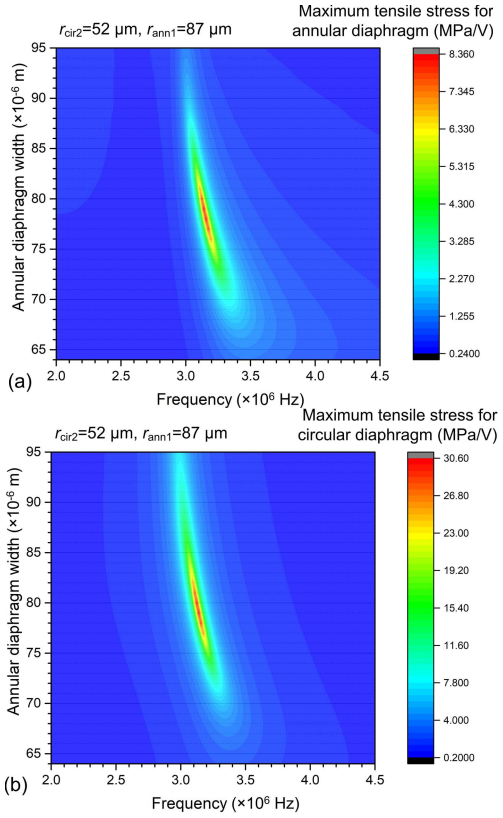

Fig. 16. Maximum silicon tensile stress–frequency response of the AC-PMUT cell. (a) Frequency response of the maximum tensile stress of the annular diaphragm. (b) Frequency response of the maximum tensile stress of the circular diaphragm.

Fig. 16(a) and (b) presents the maximum silicon tensile stress of the annular and circular diaphragms with the annular diaphragm width ranging from 64 to 95 μm. As illustrated in Fig. 16(a) and (b), the maximum tensile stress concentration on the circular diaphragm is much larger than that on the annular diaphragm. The AC-PMUT cell with the annular diaphragm width of 79 μm can still keep its maximum tensile stress under 130 MPa with ±3.7 V excitation. Moreover, this excitation voltage can be achieved by most cell phone batteries.

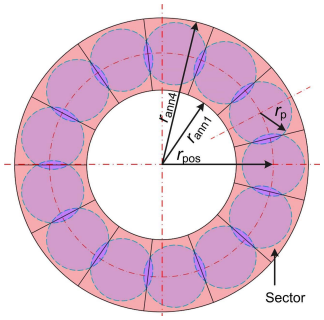

Fig. 17. Schematic of the multimodal model by breaking the annular diaphragm into an annular array consisting of equally spaced sector diaphragms and its equivalent piston radiation.

IV. Circuit Model for AC-PMUT Array

In this section, an equivalent circuit model for the AC-PMUT array is established by considering the multivibration modes of the annular diaphragm.

A. Model Establishment

Unlike the annular diaphragm working individually, the acoustic load applied on an annular diaphragm working in an array is not axisymmetric to its diaphragm axis. The unevenly distributed acoustic load makes the first bending vibration mode no longer the dominant vibration of the annular diaphragm. Instead, the higher vibration modes of the annular diaphragm become more obvious when working in an array.

Considering the multivibration modes of the annular diaphragm, the array model based on the piston vibration cannot fully describe the vibration mechanism of the annular diaphragm. In order to solve this problem, a multimodal model is presented, considering the multivibrate modes of an annular diaphragm. In this model, the annular diaphragm is separated into N_0 sectors, as shown in Fig. 17. Each annular diaphragm is equivalent to an annular array consisting of N_0 sector diaphragms [37]. Based on Hooke's law, the mechanical impedance of each sector diaphragms Z_{Sm} is $1/N_0$ times that of the annular one.

The equivalent circuit of the multimodal modal is presented in Fig. 18. In this circuit, C_{sec} is the clamped dc capacitances of each sector, which is $1/N_0$ of C_{ann}, η_{sec} is the electromechanical transduction ratios of each sector, which is equal to η_{ann}, $p_{\mathrm{cir}\,i}$ is the loaded pressure of the circular diaphragm included in the ith AC-PMUT cell, $u_{\mathrm{sec}\,ij}$ and $p_{\mathrm{sec}\,ij}$ are the volumetric velocity and loaded pressure of the ith sector included in the annular diaphragm of the jth AC-PMUT cell, respectively, and z_{sec} is the self-radiation impedance of each sector.

Considering that the dimensions of the sector are much less than the wavelength, its radiation performance can be equivalent to the vibration of a circular piston with the same volumetric displacement. In addition, these equivalent pistons forming into an annular array can be modeled by the array model for the circular cells presented in [24]. The equivalent piston radius r_{p}, the distribution radius r_{pos}, and the amount of the pistons N_0 can be calibrated by the piston vibration

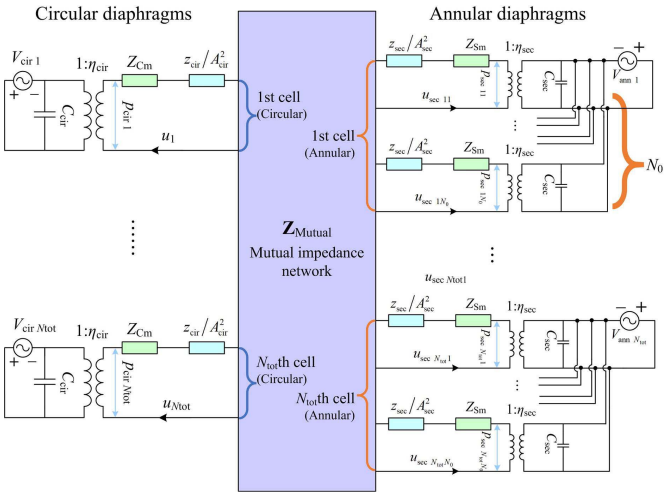

Fig. 18. Equivalent circuit model of the AC-PMUT array based on the multimodal model.

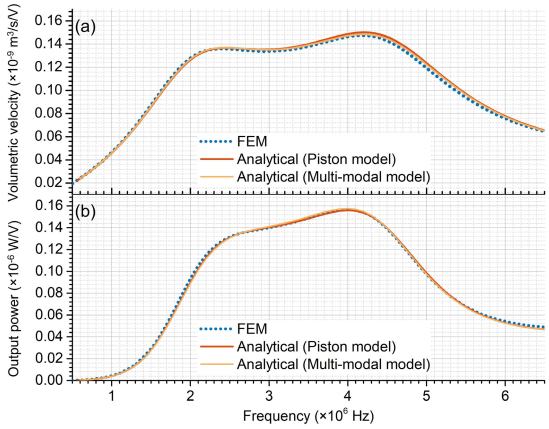

Fig. 19. Frequency response results derived from the piston model, multimodal model, and FEM. (a) Frequency response of volumetric velocity. (b) Frequency response of output power.

model of a single annular diaphragm [37]. Based on the calibration, $N_0 = 13$, $r_{\mathrm{p}} = [A_{\mathrm{ann}}/(N_0\pi)]^{0.5} = (A_{\mathrm{sec}}/\pi)^{0.5}$, and $r_{\mathrm{pos}} = 1.01\cdot(r_{\mathrm{ann4}}+r_{\mathrm{ann1}})/2$ for the annular diaphragm structure presented in Table III. The frequency-response results for the volumetric velocity and output power derived from the piston model, calibrated multimodal model, and FEM are presented in Fig. 19, and all results agree well with each other.

By this means, the AC-PMUT array is turned into a model for an array composed by $N_{\mathrm{tot}} \cdot (1 + N_0)$ equivalent piston cells with two different radii. The first N_{tot} cells have an effective radius of r_{eff} and a mechanical impedances of Z_{Cm}. The rest of the cells have an effective radius of r_{p} and mechanical impedances of Z_{Sm}. The relationship between the volumetric velocity and the radiation load on each cell can be presented as follows:

$$\begin{bmatrix} \mathbf{p}_{\mathrm{cir}} \\ \mathbf{p}_1 \\ \vdots \\ \mathbf{p}_{N_{\mathrm{tot}}} \end{bmatrix} = (\mathbf{Z}_{\mathrm{Self}} + \mathbf{Z}_{\mathrm{Mutual}}) \cdot \begin{bmatrix} \mathbf{u}_{\mathrm{cir}} \\ \mathbf{u}_1 \\ \vdots \\ \mathbf{u}_{N_{\mathrm{tot}}} \end{bmatrix} \tag{11}$$

where

$$\mathbf{p}_{\text{cir}}^{\text{T}} = [p_{\text{cir}\,1} \quad p_{\text{cir}\,2} \quad \cdots \quad p_{\text{cir}N\text{tot}}] \tag{12}$$

$$\mathbf{p}_i^{\text{T}} = [p_{\text{sec}i1} \quad p_{\text{sec}i2} \quad \cdots \quad p_{\text{sec}iN0}], \quad i \in [1, N_{\text{tot}}] \cap \mathbb{N} \tag{13}$$

$$\mathbf{u}_{\text{cir}}^{\text{T}} = [u_{\text{cir}\,1} \quad u_{\text{cir}\,2} \quad \cdots \quad u_{\text{cir}N\text{tot}}] \tag{14}$$

$$\mathbf{u}_i^{\text{T}} = [u_{\text{sec}i1} \quad u_{\text{sec}i2} \quad \cdots \quad u_{\text{sec}iN0}], \quad i \in [1, N_{\text{tot}}] \cap \mathbb{N}. \tag{15}$$

The self- and mutual-radiation impedance matrices can be presented as follows:

$$\mathbf{Z}_{\text{Self}} = \text{diag}\left[\frac{z_{\text{cir}}}{A_{\text{cir}}^2} \quad \cdots \quad \frac{z_{\text{cir}}}{A_{\text{cir}}^2} \;\middle|\; \frac{z_{\text{sec}}}{A_{\text{sec}}^2} \quad \cdots \quad \frac{z_{\text{sec}}}{A_{\text{sec}}^2}\right] \tag{16}$$

$$\mathbf{Z}_{\text{Mutual}} = \left[\begin{array}{ccc|ccc} 0 & \cdots & \frac{z_{1N\text{tot}}}{A_{\text{cir}}^2} & \frac{z_{(1)(N\text{tot}+1)}}{A_{\text{cir}}A_{\text{sec}}} & \cdots & \frac{z_{(1)(N\text{tot}+N0\cdot N\text{tot})}}{A_{\text{cir}}A_{\text{sec}}} \\ & \ddots & \vdots & \vdots & \ddots & \vdots \\ & & 0 & \frac{z_{(N\text{tot})(N\text{tot}+1)}}{A_{\text{cir}}A_{\text{sec}}} & \cdots & \frac{z_{(N\text{tot})(N\text{tot}+N0\cdot N\text{tot})}}{A_{\text{cir}}A_{\text{sec}}} \\ \hline & & & 0 & \cdots & \frac{z_{(N\text{tot}+1)(N\text{tot}+N0\cdot N\text{tot})}}{A_{\text{sec}}^2} \\ & & & & \ddots & \vdots \\ & & & & & 0 \end{array}\right] \tag{17}$$

where $\mathbf{Z}_{\text{Self}}$ is an $N_{\text{tot}} \cdot (1 + N_0)$-dimensional diagonal matrix. The nonzero elements in the first N_{tot} line are contributed by the circular diaphragms of the AC-PMUT cells, and the remaining nonzero elements are contributed by the equivalent piston for the equivalent sector diaphragms. $\mathbf{Z}_{\text{Mutual}}$ is also an $N_{\text{tot}} \cdot (1 + N_0)$-dimensional symmetric matrix and the first and fourth quadrants of the matrix are contributed by the interaction between two identical circular diaphragms and between two identical sector diaphragms, respectively. The second and third quadrants are contributed by the interaction between the circular diaphragm and the equivalent sector diaphragm. In addition, the mutual radiation impedance z_{ij} can be presented as follows:

$$z_{ij} = 2\rho c\pi r_i^2 \times \sum_{p=0}^{\infty}\left\{\frac{1}{\pi^{1/2}}\Gamma\left(p+\frac{1}{2}\right) \cdot \left(\frac{r_i}{d_{ij}}\right)^p \left[\left(\frac{\pi}{2kd_{ij}}\right)^{1/2} \cdot H_{p+1/2}^{(2)}(kd_{ij})\right] \times \sum_{n=0}^{p}\left(\frac{r_j}{r_i}\right)^{n+1}\left(\frac{J_{p-n+1}(kr_i)\cdot J_{n+1}(kr_j)}{n!(p-n)!}\right)\right\} \tag{18}$$

where r_i and r_j are the effective radii of the ith and jth cells, respectively. In addition, d_{ij} is the distance between the center of the two cells and $H_x^{(2)}$ is the spherical Hankel function of the second kind.

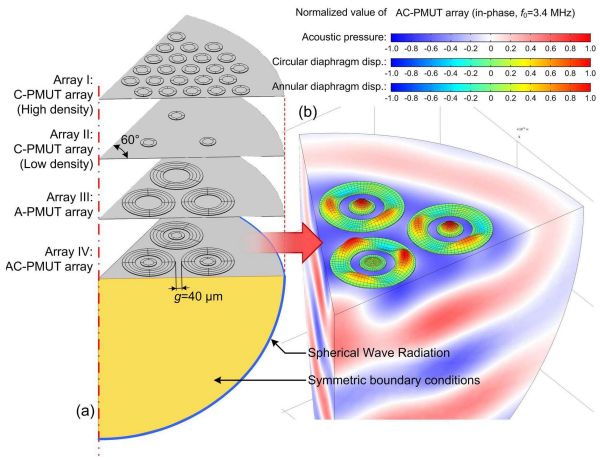

Fig. 20. Schematics of the array model used for model verification. (a) Cell distribution in four kinds of arrays. (b) Mode shape of the annular and circular diaphragms excited in the same phase at 3.4 MHz.

In the transmission mode, the volumetric velocity of each cell needs to be solved, which can be calculated by writing Kirchhoff's voltage law (KVL) equations for the circuit model presented in Fig. 18. Knowing the input voltages, the volumetric velocity matrix can be written in a matrix-form equation as follows:

$$\mathbf{u} = (\mathbf{Z}_{\text{Mech}} + \mathbf{Z}_{\text{Self}} + \mathbf{Z}_{\text{Mutual}})^{-1} \cdot \mathbf{V} \tag{19}$$

where

$$\mathbf{Z}_{\text{Mech}} = \text{diag}[Z_{\text{Cm}} \quad \cdots \quad Z_{\text{Cm}} \quad Z_{\text{Sm}} \quad \cdots \quad Z_{\text{Sm}}] \tag{20}$$

$$\mathbf{u}^{\text{T}} = \left[\mathbf{u}_{\text{cir}}^{\text{T}} \quad \mathbf{u}_{\text{sec}\,1}^{\text{T}} \quad \cdots \quad \mathbf{u}_{\text{sec}\,N_{\text{tot}}}^{\text{T}}\right] \tag{21}$$

$$\mathbf{u}_{\text{cir}}^{\text{T}} = \left[u_{\text{cir}1} \quad \cdots \quad u_{\text{cir}N_{\text{tot}}}\right] \tag{22}$$

$$\mathbf{u}_{\text{sec}\,j}^{\text{T}} = \left[u_{\text{sec}\,1j} \quad \cdots \quad u_{\text{sec}\,N_0 j}\right], \quad j \in [1, N_{\text{tot}}] \cap \mathbb{N} \tag{23}$$

$$\mathbf{V}^{\text{T}} = \left[\mathbf{V}_{\text{cir}}^{\text{T}} \quad \mathbf{V}_{\text{sec}\,1}^{\text{T}} \quad \cdots \quad \mathbf{V}_{\text{sec}\,N_{\text{tot}}}^{\text{T}}\right] \tag{24}$$

$$\mathbf{V}_{\text{cir}}^{\text{T}} = \left[\eta_{\text{cir}}V_{\text{cir}1} \quad \cdots \quad \eta_{\text{cir}}V_{\text{cir}N_{\text{tot}}}\right] \tag{25}$$

$$\mathbf{V}_{\text{sec}\,j}^{\text{T}} = V_{\text{ann}j} \cdot [\eta_{\text{ann}} \quad \cdots \quad \eta_{\text{ann}}], \quad j \in [1, N_{\text{tot}}] \cap \mathbb{N}. \tag{26}$$

The acoustic field of the array can also be derived based on the superimposing of the acoustic field generated by each equivalent piston [41].

B. Array Model Verification

In this section, COMSOL Multiphysics v5.3 is used as the FEM simulation tool to verify the analytical model. Tables II and III summarize the detailed material and structural parameters of the annular and circular diaphragms used in array analysis, respectively. The verification and performance comparisons are conducted on the basis of a series of small-scale 2-D array, as shown in Fig. 20. Except Array II, the smallest gap between every two cells is all set as 40 μm. In addition, the coordinates of each cell in Arrays II–IV are the same. Choosing one-sixth of the model can not only save the calculating resources but also avoid the interception of the symmetric boundary across the PMUT diaphragm which could interfere with the diaphragms' vibration mode shapes.

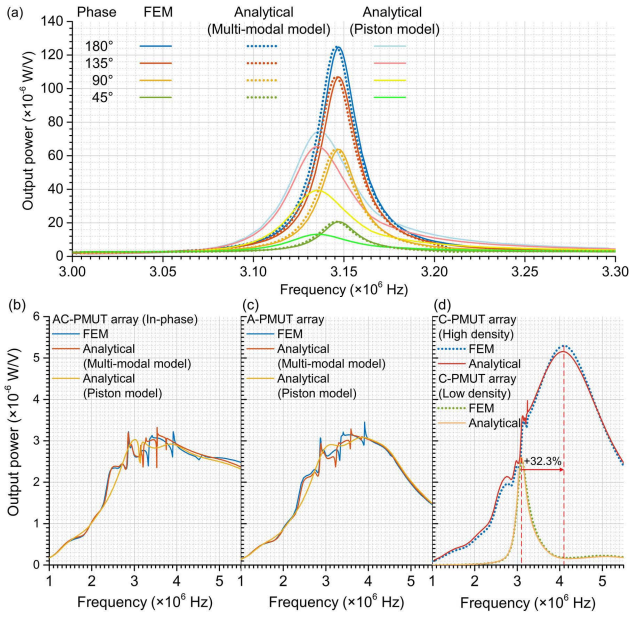

Fig. 21. Verification for frequency response of the output power. (a) Frequency response generated by the AC-PMUT array with the excitation phase ranging from 45° to 180°. (b) Frequency response generated by the in-phase-excited AC-PMUT array. (c) Frequency response generated by the A-PMUT array. (d) Frequency response generated by the C-PMUT array with high and low distribution densities.

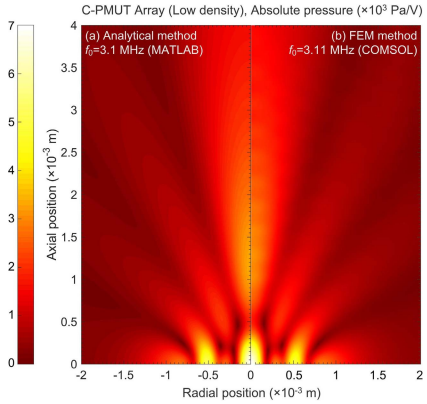

Fig. 22. Spatial distribution of the output pressure generated by Array II in its resonant frequency. (a) Multimodal model result. (b) FEM result.

Fig. 21(a) presents the frequency response of the output power generated by the AC-PMUT array with different excitation phases between the annular and circular diaphragms. Fig. 21(a) indicates that the coaxially positioned annular and circular diaphragms excited in an antiphase mode can achieve the highest output sensitivity. In addition, the proposed multimodal model derived results achieve good agreement with the FEM-derived results, while the extra restriction of the piston model making the whole annular diaphragm surface vibrate uniformly stiffens the diaphragm and underestimates its output power.

As shown in Fig. 21(b), when the two diaphragms of AC-PMUT are excited in-phase, the coupling within one cell is impaired and the crosstalk between different cells is enhanced. The crosstalk impacts the system to produce

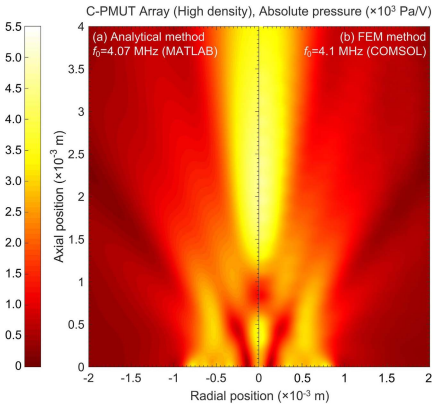

Fig. 23. Spatial distribution of the output pressure generated by Array I in its resonant frequency. (a) Multimodal model result. (b) FEM result.

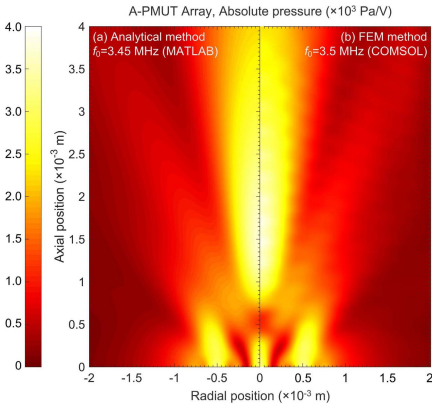

Fig. 24. Spatial distribution of the output pressure generated by Array III in its resonant frequency. (a) Multimodal model result. (b) FEM result.

multiple spurious resonant frequencies [30] and increases the system bandwidth but suppresses the volumetric displacement of each cell. In addition, the output power–frequency response generated by Array III presented in Fig. 21(c) shows a similar frequency response with that presented in Fig. 21(b). According to Fig. 21(b) and (c), although the piston model can approximately approach the output power of the array, the overconstrained assumption makes its frequency response profile smoother than that derived by FEM. The multimodal model can give a better approach than the piston model.

Fig. 21(d) presents the frequency response generated by the C-PMUT array with high (Array I) and low (Array II) distribution densities. Array II having a larger distance between the two cells reduces the mutual radiation impedance between them and ultimately reduces the crosstalk. With a smaller crosstalk, the frequency of Array II achieving the largest output power keeps consistent with the resonant frequency of each cell. On the contrary, the high vibration amplitude of each cell at its resonant frequency in Array I not only fails to improve the output pressure but also enhances the crosstalk in the array. The heavy crosstalk effect drives a certain number of cells acoustically instead of electrically, which indicates that they are absorbing the acoustic power from the sound field radiated by other cells. This scenario reduces the output power and causes distortion of the ultrasound beam pattern. Therefore,

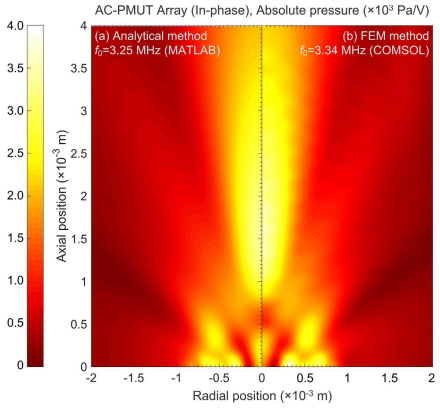

Fig. 25. Spatial distribution of the output pressure generated by Array IV excited in the same phase. (a) Multimodal model result. (b) FEM result.

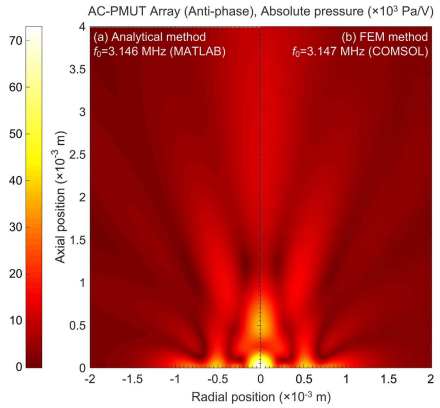

Fig. 26. Spatial distribution of the output pressure generated by Array IV excited in an antiphase mode. (a) Multimodal model result. (b) FEM result.

the C-PMUT array with a high distribution density cannot provide a stable high output at the resonant frequency of each cell. Only at a frequency higher than the resonant frequency, the crosstalk effect can be reduced due to the reduction in the vibration amplitude of each cell. Thus, the C-PMUT cells in the traditional array tend to have a rather uniform vibration phase distribution to provide a stable output performance. Fig. 21(d) also indicates that although the C-PMUT array with a low distribution density can reduce the crosstalk and improve the output efficiency of each cell, the reduced cell number also impairs its output ability. However, by using the coupling effect between the annular and circular diaphragms within one cell, the AC-PMUT array can not only reduce the crosstalk effect but also increase the output ability.

Then, the multimodal model-derived acoustic field generated by Arrays I–IV with both antiphase- and in-phase-excitation methods is verified. As shown from Figs. 22–26, the multimodal model-derived results agree well with that derived by FEM.

Finally, the absolute acoustic pressure generated along the array axis and at the Rayleigh distance of the array is presented in Figs. 27 and 28. The antiphase-excited AC-PMUT array achieves the highest output pressure among other array designs. In addition, the C-PMUT array with a high distribution density also achieves a good output performance, even

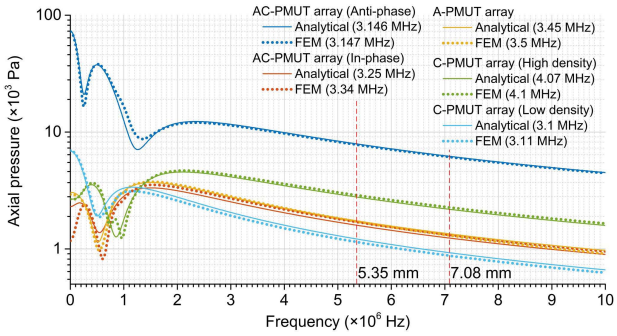

Fig. 27. Comparison of axial pressure distributions among the antiphase-excited AC-PMUT array, in-phase-excited AC-PMUT array, A-PMUT array, and C-PMUT array with high and low distribution densities.

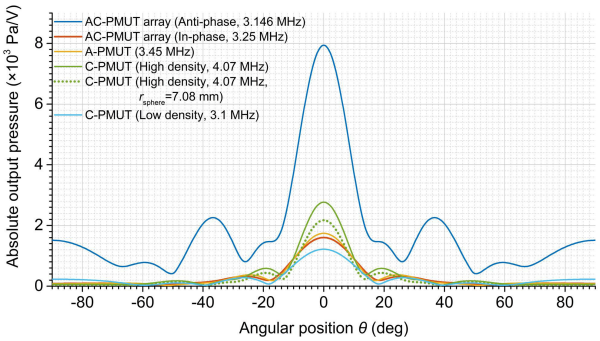

Fig. 28. Comparison of averaged pressure distribution at the Rayleigh distance [41] for each array, which is around 5.35 and 7.08 mm for the array working around 3.1 and 4.1 MHz, respectively.

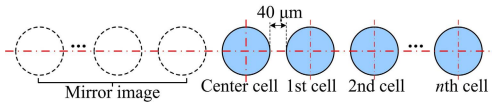

Fig. 29. Schematics for the cell distribution in 1-D array.

better than the performance of the in-phase-excited AC-PMUT array.

V. Array Performance Discussion

Based on the multimodal model, this section compares the crosstalk intensity and ultrasound emission performance of the C-PMUT and AC-PMUT arrays. The optimized AC-PMUT cell presented in Section III is selected as the cell for the AC-PMUT array.

A. Crosstalk Performance of 1-D Array

In this section, the proposed AC-PMUT and traditional C-PMUT ($r_{cir2} = 52\ \mu$m) form a 1-D array. A 40-μm gap is provided between every two cells, as shown in Fig. 29. By adding the cell number from 1 to 11, the crosstalk behaviors of the two 1-D arrays are compared, as illustrated in Fig. 30. Fig. 30(a) and (b) shows the output power–frequency responses of each cell in these two arrays as the cell numbers increase.

Compared with the C-PMUT array, the proposed AC-PMUT array remarkably reduces the crosstalk effect in the array.

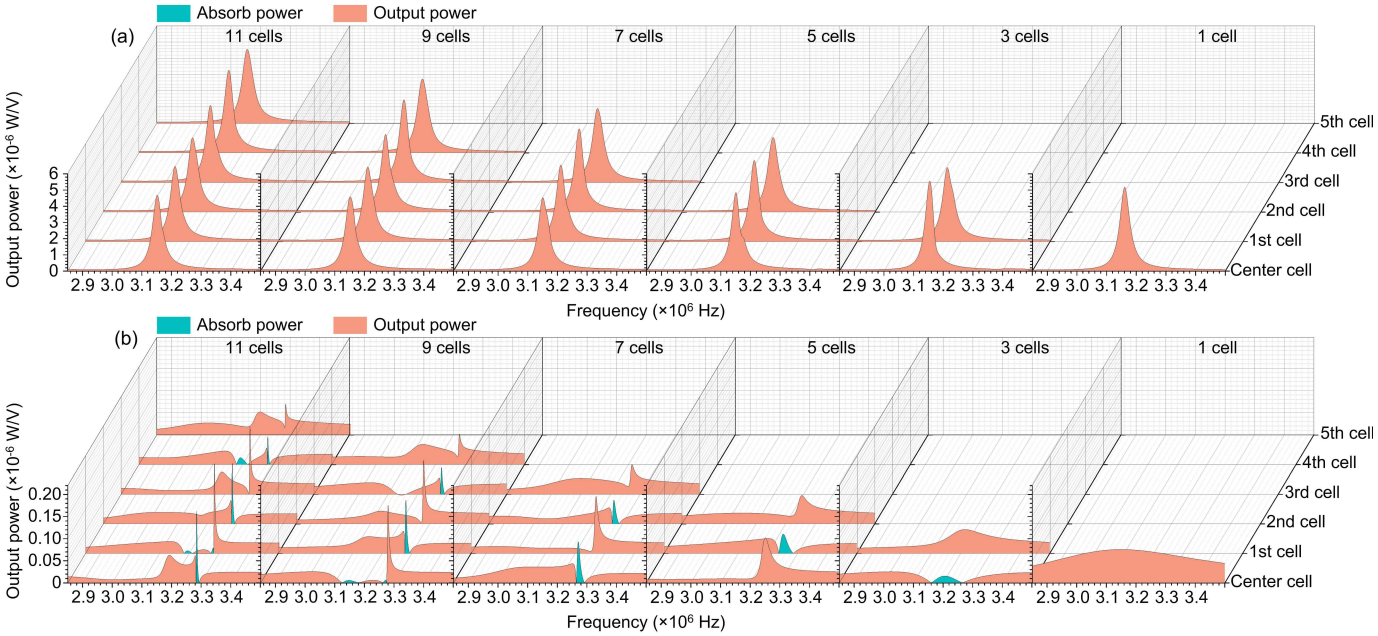

Fig. 30. Output power–frequency response of each cell in 1-D array with different amounts of cells. (a) Array consisting of the proposed AC-PMUT cells. (b) Array consisting of the traditional C-PMUT cells.

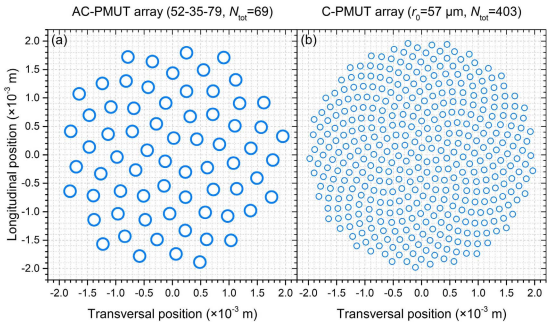

Fig. 31. Cell distributions in the arrays. (a) Distribution for AC-PMUT array. (b) Distribution for C-PMUT array.

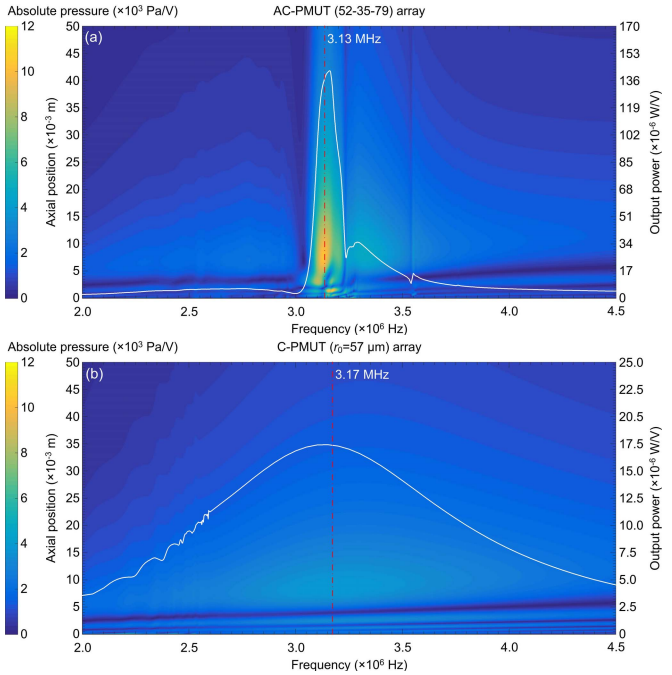

Fig. 32. Frequency response versus output pressure and power of PMUTs with the proposed and traditional array. (a) Frequency response of the AC-PMUT array. (b) Frequency response of the C-PMUT array.

The output power–frequency response of each cell can nearly maintain the same profile as that when they are working individually. However, the output power–frequency responses of the traditional C-PMUT cells are very distorted. The spurious resonance in the frequency response of the output power is mainly caused by the propagation mechanism of the Rayleigh–Bloch (RB) surface waves [30]. Some cells even show negative output power meaning that these corresponding cells are absorbing the acoustic energy instead of emission, as the blue color illustrated in Fig. 30(b).

B. Emission Performance of 2-D Array

The performances of the large-scale 2-D arrays are analyzed in this part. Because of the existing heavy crosstalk effect of the traditional C-PMUT array, its working frequency achieving the highest output ability is usually higher than the resonant frequency of an individual C-PMUT cell, as the discussion in Fig. 21(d). Therefore, a C-PMUT cell with a radius of 57 μm with the same layer thicknesses is selected as the cell for the C-PMUT array, in order to make the array achieve the highest output power around 3 MHz. By this means, a fair performance comparison can be conducted between the AC-PMUT and C-PMUT arrays. In addition, the cell distribution follows the pattern of Fermat's array [48], [49], as shown in Fig. 31.

1) Nonfocusing Working Condition: Initially, both arrays are analyzed under a nonfocusing working condition within a frequency ranging from 2 to 4.5 MHz. The frequency responses versus the ultrasonic output pressure of the arrays along its axis

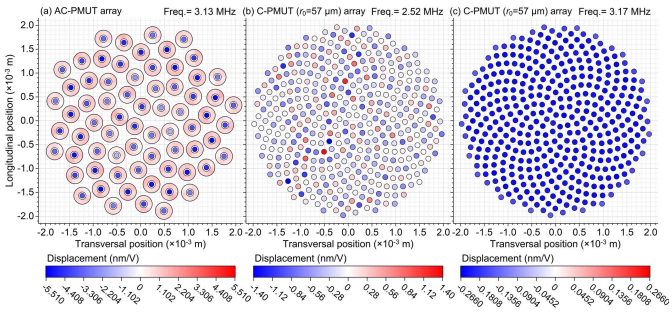

Fig. 33. Displacement of each diaphragm in the arrays when the excitation signal reaches its 90° phase. (a) Displacement condition of the diaphragms in the AC-PMUT array when working at its resonant working frequency. (b) Displacement condition of the diaphragms in the C-PMUT array when working at the resonant frequency of a single cell. (c) Displacement condition of the diaphragms in the C-PMUT array when achieving the highest output pressure.

are analyzed and presented in Fig. 32(a) and (b). Fig. 32(a) indicates that the proposed AC-PMUT array achieves the highest output pressure around its resonant frequency of 3.13 MHz. Considering the low crosstalk effect, all AC-PMUT cells in the proposed array can work uniformly at the resonant frequency. On this basis, the phenomenon of the output pressure offset among different cells has been reduced, and the AC-PMUT array can fully use the large vibration amplitude to achieve a stable resonant condition.

However, as the discussion presented for Fig. 21(d), Fig. 32(b) indicates that the C-PMUT array cannot provide a stable high output pressure at its resonant frequency, around 2.5 MHz. Only at a higher frequency, can the cells in the C-PMUT array tend to have a further uniform vibration condition across the array to provide a stable output performance.

A video presenting the displacement of each diaphragm in the arrays is provided in the attachment. Assuming that a sinusoidal signal was applied to excite the AC- and C-PMUT arrays, the video records the vibration displacement of each diaphragm under the steady operating condition at each working frequency, when the excitation signal reaches its 90° phase.

The displacement condition of the antiphase-excited AC-PMUT array at its resonant frequency of 3.13 MHz is presented in Fig. 33(a), which indicates that all the cells are working in a quite uniform condition across the array. Fig. 33(b) presents the displacement condition of the C-PMUT array at the frequency of 2.52 MHz, which is the resonant frequency of a C-PMUT cell ($r_{\text{cir2}} = 57\ \mu\text{m}$). Fig. 33(c) presents the displacement condition of the C-PMUT array at the frequency of 3.17 MHz, at which frequency the C-PMUT array achieves the highest output pressure. Fig. 33(b) and (c) verifies the results derived from Fig. 32(b), indicating that only at the higher working frequency with a more uniform working condition for the cells across the array can the C-PMUT array achieve a stable and high output ability.

Fig. 34 presents the spatial distribution of the output pressure generated by these two arrays in their working conditions with the highest output pressure. The AC-PMUT array achieves the highest output pressure value along the array axis, increased by 166% compared with that generated by the C-PMUT array.

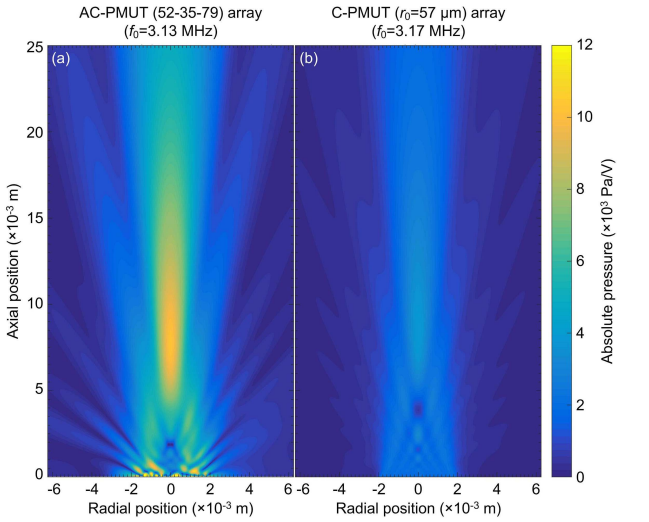

Fig. 34. Spatial distribution of output pressure generated by PMUT array working in nonfocusing working condition. (a) Output pressure distribution generated by AC-PMUT array in its working frequency with the maximum output pressure. (b) Output pressure distribution generated by the C-PMUT array in its working frequency with the maximum output pressure.

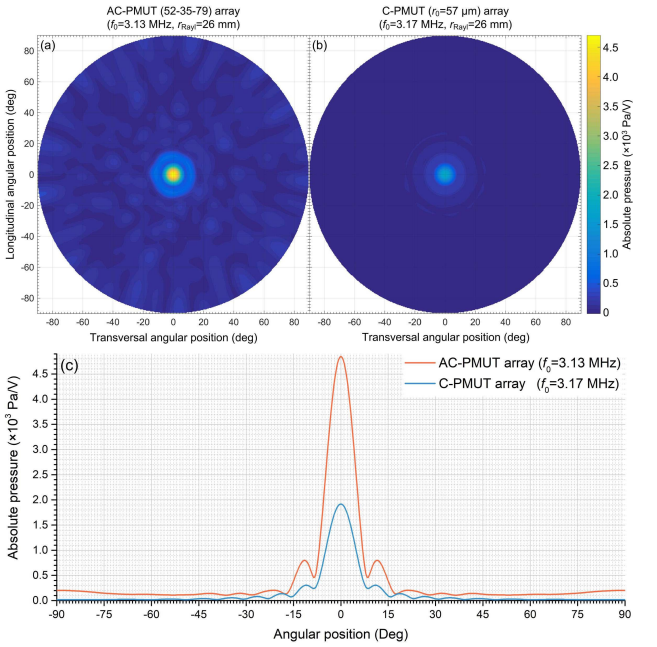

Fig. 35. Far-field performance of the array. (a) Pressure distribution on the spherical surface (radius = 26 mm) of the AC-PMUT array with a working frequency of 3.13 MHz. (b) Pressure distribution on the spherical surface (radius = 26 mm) of the C-PMUT array with a working frequency of 3.17 MHz. (c) Comparison of averaged pressure distribution at the Rayleigh distance [41] for each array.

Fig. 35(a) and (b) shows the pressure distribution on a hemisphere with a Rayleigh distance of 26 mm from the center of the array, which is the beginning of the far field [41]. Fig. 35(c) presents a comparison of the average output pressure values generated by these two arrays at their Rayleigh distance. Similar to the analysis above, the pressure generated by the AC-PMUT array achieves a 153% increase compared with the C-PMUT array at the Rayleigh distance.

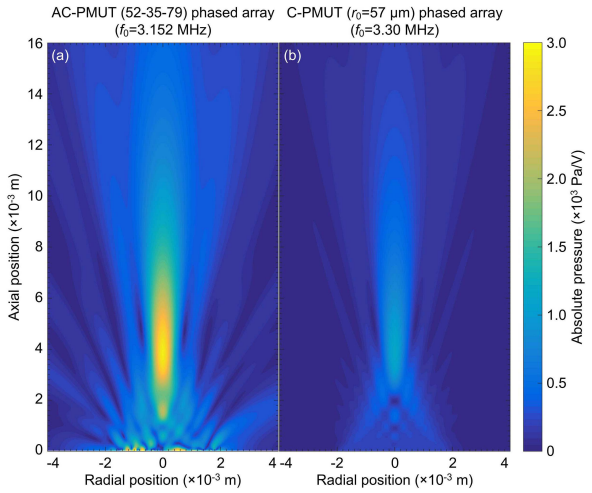

Fig. 36. Spatial distribution of output pressure generated by the AC- and C-PMUT arrays working in the phased-array condition. (a) Output pressure distribution generated by the AC-PMUT phased array. (b) Output pressure distribution generated by the C-PMUT phased array.

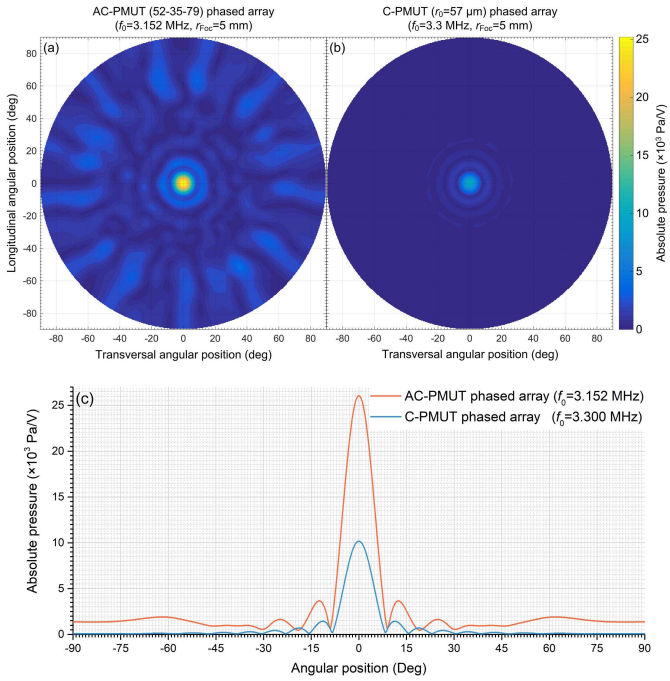

Fig. 37. Pressure distribution at the hemisphere with a radius of 5 mm. (a) Output pressure distribution of the AC-PMUT array on the hemispherical surface with a radius of 5 mm. (b) Output pressure distribution of the C-PMUT array on the hemispherical surface with a radius of 5 mm. (c) Comparison of averaged pressure distribution at a position of 5 mm.

2) Focusing Working Condition: The output pressure of the array can be further improved with a strong mainlobe amplitude and a narrow beamwidth by electronic focusing. The focal length is set to 5 mm. In addition, the spatial distribution of the output pressure generated by these two phased arrays in their working conditions with the highest output pressure is compared and presented in Fig. 36. Fig. 37 shows the focused output pressure distribution of both arrays on the surface of the hemisphere with a radius of 5 mm. Notably, the phased-array method can increase the output pressure and shrink the mainlobe width. According to the directivities at 5-mm distance, as illustrated in Fig. 37(c), the AC-PMUT array achieves an output pressure increase of 155% compared with the maximum pressure value generated by the C-PMUT array.

According to the analysis above and the principle of energy conservation, although the coupled AC-PMUT design helps to enhance the output ability, its bandwidth has been impaired, which is not desirable for the imaging application. However, considering the high output performance and low crosstalk ability of the proposed AC-PMUT cell, an array with AC-PMUT cells in different dimensions may be helpful to extend its bandwidth. Considering the current design for the AC-PMUT cell and array, they can always achieve its maximum output pressure when working in its resonant frequency due to the low crosstalk effect. This characteristic of the AC-PMUT array can be especially useful as an active sonar system, which requires transducers to play as projectors and hydrophone operators in the vicinity of the same resonant frequency [42].

VI. Conclusion

This study presents an equivalent circuit model for the PMUT cell and array consisting of annular and circular diaphragms. Based on the proposed model, a PMUT cell structure composed of a pair of coaxially positioned annular and circular diaphragms, with a separate driving system, has been presented. Based on the continuity equation of the fluid, these two diaphragms are excited in an antiphase mode to enhance the coupling between them within one cell. Moreover, this crosstalk within one cell not only reduces the mutual crosstalk effect across the array but also helps the array to achieve a high ultrasonic emission performance. In addition, the proposed model can give an efficient design and optimization for the PMUT cell and array, considering the multiphysics coupling among the electrical, mechanical, and acoustical domains. In summary, a detailed analysis is conducted for the output performance of the AC-PMUT array, which can make full use of the large amplitude generated by each cell, given the low-crosstalk effect. As a result, the resonant mode of the AC-PMUT array is achieved to obtain a much higher output pressure than that of the traditional C-PMUT array.

References

[1] B. W. Drinkwater and P. D. Wilcox, "Ultrasonic arrays for non-destructive evaluation: A review," *NDT E Int.*, vol. 39, no. 7, pp. 525–541, Oct. 2006.

[2] X. Chen *et al.*, "A high accuracy transit-time airflow volumetric flowmeter based on pMUTs arrays," in *Proc. IEEE 32nd Int. Conf. Micro Electro Mech. Syst. (MEMS)*, Jan. 2019, pp. 743–746.

[3] A. J. Tajik *et al.*, "Two-dimensional real-time ultrasonic imaging of the heart and great vessels. Technique, image orientation, structure identification, and validation," in *Proc. Mayo Clinic*, 1978, pp. 271–303.

[4] S. Mitragotri, "Healing sound: The use of ultrasound in drug delivery and other therapeutic applications," *Nature Rev. Discovery*, vol. 4, no. 3, pp. 255–260, 2005.

[5] D. L. Miller *et al.*, "Overview of therapeutic ultrasound applications and safety considerations," *J. Ultrasound Med.*, vol. 31, no. 4, pp. 623–634, Apr. 2012.

[6] G. Ogris, T. Stiefmeier, H. Junker, P. Lukowicz, and G. Troster, "Using ultrasonic hand tracking to augment motion analysis based recognition of manipulative gestures," in *Proc. 9th IEEE Int. Symp. Wearable Comput. (ISWC)*, Oct. 2005, pp. 152–159.

[7] H.-Y. Tang *et al.*, "3-D ultrasonic fingerprint sensor-on-a-chip," *IEEE J. Solid-State Circuits*, vol. 51, no. 11, pp. 2522–2533, Nov. 2016.

[8] R. J. Przybyla *et al.*, "3D ultrasonic gesture recognition," in *IEEE Int. Solid-State Circuits Conf. (ISSCC) Dig. Tech. Papers*, Feb. 2014, pp. 210–211.

[9] B. Khuri-Yakub, O. Oralkan, and M. Kupnik, "Next-gen ultrasound," *IEEE Spectr.*, vol. 46, no. 5, pp. 44–54, May 2009.

[10] J. F. Dias, "Construction and performance of an experimental phased array acoustic imaging transducer," *Ultrason. Imag.*, vol. 3, no. 4, pp. 352–368, Oct. 1981.

[11] J. Jung, W. Lee, W. Kang, E. Shin, J. Ryu, and H. Choi, "Review of piezoelectric micromachined ultrasonic transducers and their applications," *J. Micromech. Microeng.*, vol. 27, no. 11, Nov. 2017, Art. no. 113001.

[12] K. K. Shung and M. Zippuro, "Ultrasonic transducers and arrays," *IEEE Eng. Med. Biol. Mag.*, vol. 15, no. 6, pp. 20–30, Nov./Dec. 1996.

[13] Y. Qiu *et al.*, "Piezoelectric micromachined ultrasound transducer (PMUT) arrays for integrated sensing, actuation and imaging," *Sensors*, vol. 15, no. 4, pp. 8020–8041, Apr. 2015.

[14] M. Wang, Y. Zhou, and A. Randles, "Enhancement of the transmission of piezoelectric micromachined ultrasonic transducer with an isolation trench," *J. Microelectromech. Syst.*, vol. 25, no. 4, pp. 691–700, Aug. 2016.

[15] S. Akhbari *et al.*, "Bimorph piezoelectric micromachined ultrasonic transducers," *J. Microelectromech. Syst.*, vol. 25, no. 2, pp. 326–336, 2016.

[16] S. Akhbari, F. Sammoura, S. Shelton, C. Yang, D. Horsley, and L. Lin, "Highly responsive curved aluminum nitride pMUT," in *Proc. IEEE 27th Int. Conf. Micro Electro Mech. Syst. (MEMS)*, Jan. 2014, pp. 124–127.

[17] S. Shelton, O. Rozen, A. Guedes, R. Przybyla, B. Boser, and D. A. Horsley, "Improved acoustic coupling of air-coupled micromachined ultrasonic transducers," in *Proc. IEEE 27th Int. Conf. Micro Electro Mech. Syst. (MEMS)*, Jan. 2014, pp. 753–756.

[18] B. Eovino, S. Akhbari, and L. Lin, "Ring shaped piezoelectric micromachined ultrasonic transducers (PMUT) with increased pressure generation," in *Proc. Hilton Head*, 2016, pp. 432–445.

[19] B. E. Eovino, S. Akhbari, and L. Lin, "Broadband ring-shaped PMUTS based on an acoustically induced resonance," in *Proc. IEEE 30th Int. Conf. Micro Electro Mech. Syst. (MEMS)*, Jan. 2017, pp. 1184–1187.

[20] Q. Wang, Y. Kusano, and D. A. Horsley, "Coupled piezoelectric micromachined ultrasonic transducers with improved pulse-echo performance," in *Proc. IEEE 30th Int. Conf. Micro Electro Mech. Syst. (MEMS)*, Jan. 2017, pp. 151–154.

[21] B. Bayram *et al.*, "Finite element modeling and experimental characterization of crosstalk in 1-D CMUT arrays," *IEEE Trans. Ultrason., Ferroelectr., Freq. Control*, vol. 54, no. 2, pp. 418–430, Feb. 2007.

[22] C. Meynier, F. Teston, and D. Certon, "A multiscale model for array of capacitive micromachined ultrasonic transducers," *J. Acoust. Soc. Amer.*, vol. 128, no. 5, pp. 2549–2561, Nov. 2010.

[23] M. Berthillier, P. Le Moal, and J. Lardies, "Comparison of various models to compute the vibro-acoustic response of large CMUT arrays," in *Proc. Acoust. Nantes Conf.*, 2012, pp. 3125–3130.

[24] H. K. Oguz, A. Atalar, and H. Köymen, "Equivalent circuit-based analysis of CMUT cell dynamics in arrays," *IEEE Trans. Ultrason., Ferroelectr., Freq. Control*, vol. 60, no. 5, pp. 1016–1024, May 2013.

[25] J. D. Larson, "Non-ideal radiators in phased array transducers," in *Proc. Ultrason. Symp.*, 1981, pp. 673–684.

[26] X. Jin, O. Oralkan, F. L. Degertekin, and B. T. Khuri-Yakub, "Characterization of one-dimensional capacitive micromachined ultrasonic immersion transducer arrays," *IEEE Trans. Ultrason., Ferroelectr., Freq. Control*, vol. 48, no. 3, pp. 750–760, May 2001.

[27] A. Caronti, A. Savoia, G. Caliano, and M. Pappalardo, "Acoustic coupling in capacitive microfabricated ultrasonic transducers: Modeling and experiments," *IEEE Trans. Ultrason., Ferroelectr., Freq. Control*, vol. 52, no. 12, pp. 2220–2234, Dec. 2005.

[28] J. Zhang, W. J. Hughes, R. J. Meyer, K. Uchino, and R. E. Newnham, "Cymbal array: A broad band sound projector," *Ultrasonics*, vol. 37, no. 8, pp. 523–529, Jan. 2000.

[29] K. J. Opielinski, M. Celmer, and R. Bolejko, "Crosstalk effect in medical ultrasound tomography imaging," in *Proc. Joint Conf.-Acoust.*, Sep. 2018, pp. 1–6.

[30] A. Atalar, H. Köymen, and H. K. Oğuz, "Rayleigh–Bloch waves in CMUT arrays," *IEEE Trans. Ultrason., Ferroelectr., Freq. Control*, vol. 61, no. 12, pp. 2139–2148, Dec. 2014.

[31] B. Cugnet, A.-C. Hladky, and J. Assaad, "Numerical technique to reduce cross-coupling in acoustical arrays," *Ultrasonics*, vol. 40, nos. 1–8, pp. 503–506, May 2002.

[32] A. Bybi, S. Grondel, J. Assaad, A.-C. Hladky-Hennion, C. Granger, and M. Rguiti, "Reducing crosstalk in array structures by controlling the excitation voltage of individual elements: A feasibility study," *Ultrasonics*, vol. 53, no. 6, pp. 1135–1140, Aug. 2013.

[33] S. Akhbari, F. Sammoura, and L. Lin, "Equivalent circuit models for large arrays of curved and flat piezoelectric micromachined ultrasonic transducers," *IEEE Trans. Ultrason., Ferroelectr., Freq. Control*, vol. 63, no. 3, pp. 432–447, Mar. 2016.

[34] Q. Wang and D. A. Horsley, "Using a mutual acoustic impedance model to improve the time domain response of PMUT arrays," in *Proc. IEEE Int. Ultrason. Symp. (IUS)*, Sep. 2017, pp. 1–4.

[35] W. P. Mason, *Electromechanical Transducers and Wave Filters*. New York, NY, USA: Van Nostrand, 1942.

[36] F. V. Hunt, *Electroacoustics: The Analysis of Transduction, and Its Historical Background*. Cambridge, MA, USA: Harvard Univ. Press, 2014.

[37] T. Xu *et al.*, "An analytical equivalent circuit model for optimization design of a broadband piezoelectric micromachined ultrasonic transducer with an annular diaphragm," *IEEE Trans. Ultrason., Ferroelectr., Freq. Control*, vol. 66, no. 11, pp. 1760–1776, Nov. 2019.

[38] F. Sammoura and S.-G. Kim, "Theoretical modeling and equivalent electric circuit of a bimorph piezoelectric micromachined ultrasonic transducer," *IEEE Trans. Ultrason., Ferroelectr., Freq. Control*, vol. 59, no. 5, pp. 990–998, May 2012.

[39] K. Smyth, S. Bathurst, F. Sammoura, and S.-G. Kim, "Analytic solution for N-electrode actuated piezoelectric disk with application to piezoelectric micromachined ultrasonic transducers," *IEEE Trans. Ultrason., Ferroelectr., Freq. Control*, vol. 60, no. 8, pp. 1756–1767, Aug. 2013.

[40] T. Xu *et al.*, "Array design of piezoelectric micromachined ultrasonic transducers with low-crosstalk and high-emission performance," *IEEE Trans. Ultrason., Ferroelectr., Freq. Control*, vol. 67, no. 4, pp. 789–800, Apr. 2020.

[41] D. T. Blackstock, *Fundamentals of Physical Acoustics*. Hoboken, NJ, USA: Wiley, 2000.

[42] C. H. Sherman and J. L. Butler, *Transducers and Arrays for Underwater Sound*. Cham, Switzerland: Springer, 2007.

[43] *Ultrasound Frequencies*. Accessed: Oct. 20, 2019. [Online]. Available: https://radiopaedia.org/articles/ultrasound-frequencies

[44] T. Xu *et al.*, "Coupled piezoelectric micromachined ultrasonic transducers array with high ultrasonic emission performance," in *Proc. IEEE 13th Annu. Int. Conf. Nano/Micro Eng. Mol. Syst. (NEMS)*, Apr. 2018, pp. 151–154.

[45] M. Bao and S. Middelhoek, *Micro Mechanical Transducers: Pressure Sensors, Accelerometers and Gyroscopes*. Amsterdam, The Netherlands: Elsevier, 2000.

[46] M. Ohring and L. Kasprzak, *Reliability and Failure of Electronic Materials and Devices*. Amsterdam, The Netherlands: Elsevier, 2014.

[47] M. Ferrari, *BioMEMS and Biomedical Nanotechnology: Biological and Biomedical Nanotechnology*, vol. 1. Cham, Switzerland: Springer, 2007.

[48] O. Martínez-Graullera, C. J. Martín, G. Godoy, and L. G. Ullate, "2D array design based on fermat spiral for ultrasound imaging," *Ultrasonics*, vol. 50, no. 2, pp. 280–289, Feb. 2010.

[49] A. Ramalli, E. Boni, A. S. Savoia, and P. Tortoli, "Density-tapered spiral arrays for ultrasound 3-D imaging," *IEEE Trans. Ultrason., Ferroelectr., Freq. Control*, vol. 62, no. 8, pp. 1580–1588, Aug. 2015.

Tingzhong Xu received the B.S. degree in mechanical engineering from Xi'an Jiaotong University, Xi'an, China, in 2013. He is currently pursuing the Ph.D. degree with Xi'an Jiaotong University and the University of New South Wales, Sydney, NSW, Australia.

His research interests include the design, fabrication, and characterization of microelectromechanical system (MEMS) sensors, especially the piezoelectric micromachined ultrasonic transducers (PMUTs) for industrial and biomedical applications and ultrahigh sensitive pressure sensor for low-pressure sensing.

Libo Zhao received the M.S. and Ph.D. degrees in instrument science and technology from the Institute of Precision Engineering, Xi'an Jiaotong University, Xi'an, China, in 2003 and 2007, respectively.

He is currently a Professor with Xi'an Jiaotong University. His research interests include microfabrication and nanofabrication technology, microelectromechanical system (MEMS) sensor technology, and precision machining technology.

Zhuangde Jiang received the Ph.D. degree from the University of Birmingham, Birmingham, U.K., in 2011.

He is currently a Professor with Xi'an Jiaotong University, Xi'an, China, where he is an Academician with the Chinese Academy of Engineering. He is also currently the Director of the Institute of Precision Engineering (IPE), Xi'an Jiaotong University. He involves in research areas including microfabrication and nanofabrication technology, microelectromechanical system (MEMS) and sensor technology, ultraprecision machining technology and equipment, and photoelectric testing technology and instrumentation.

Dr. Jiang is the Vice Director of the Chinese Society of Micro-Nano Technology (CSMNT) and the Executive Director of the Chinese Mechanical Engineering Society (CMES).

Shuaishuai Guo received the B.S. degree in mechanical engineering from Qingdao University, Qingdao, China, in 2016. He is currently pursuing the master's degree in instrument engineering with Xi'an Jiaotong University, Xi'an, China.

His research interests include design and fabrication of piezoelectric micromachined ultrasonic transducers (PMUTs).

Zhikang Li received the B.S. degree in mechanical manufacturing and automation and the Ph.D. degree in mechanical engineering from Xidian University, Xi'an, China, in 2010 and 2017, respectively.

During his Ph.D. program, he was a jointly cultivated Ph.D. Student with the Group of Professor L. Lin, UC Berkeley, Berkeley, CA, USA, for one year. Since 2017, he has been a Faculty Member of the School of Mechanical Engineering, Xi'an Jiaotong University. He is currently a Lecturer with the School of Mechanical Engineering, Xi'an Jiaotong University. His research interests include capacitive micromachined ultrasonic transducers and precision machining.

Ping Yang was born in Xianyang, China, in 1986. She received the bachelor's degree in English language and literature from Northwest University, Kirkland, WA, USA, in 2009.

She is currently the Office Director of the International Joint Laboratory for Micro/Nano Manufacturing and Measurement Technologies, the Scientific Research Secretary of Academician, and the Secretary of the Department of Mechanical Engineering, Institute of Precision Engineering, Xi'an Jiaotong University, Xi'an, China. She involves in the project managements about the research fields of microfabrication and nanofabrication technologies, microelectromechanical system (MEMS) sensor technology, and photoelectric testing technology and instrumentation.

Guoxi Luo received the Ph.D. degree in instrument science and technology from Chongqing University, Chongqing, China, in 2016.

He is currently an Assistant Professor with Xi'an Jiaotong University, Xi'an, China. His research interests include microfabrication and nanofabrication technology, nanoenergy harvesting technology, and electrochemistry.

Lin Sun received the B.Sc. degree in mechanical engineering from Northeastern University, Shenyang, China, in 2012. He is currently pursuing the Ph.D. degree in mechanical engineering with Xi'an Jiaotong University, Xi'an, China.

Liangchi Zhang is currently a Scientia Professor with the School of Mechanical and Manufacturing Engineering, UNSW Sydney, Sydney, NSW, Australia. His research is in the area of advanced manufacturing.